The following article appeared in Journal of Materials Research and Technology, 9(4): 9328-9340 (2020) and may be found at: https://doi.org/10.1016/j.jmrt.2020.03.110

Available online at www.sciencedirect.com

jmr&t Journal of Materials Research and Technology

https://www.journals.elsevier.com/journal-of-materials-research-and-technology

Original article

Investigation of a Ti–30Zr binary alloy fabricated through spark plasma sintering

Jorge Chávez[a], *Luis Olmos*[a,*], *Omar Jimenez*[b], *Francisco Alvarado-Hernández*[c], *Horacio Flores-Zúñiga*[d], *Juan-Pablo Camarillo-Garcia*[d], *Santiago José Guevara-Martínez*[a]

[a] *Universidad Michoacana de San Nicolás de Hidalgo, Morelia, Mexico*
[b] *Universidad de Guadalajara, Guadalajara Mexico*
[c] *Universidad Autónoma de Zacatecas, Mexico*
[d] *Materiales Avanzados, Instituto Potosino de Investigación Científica y Tecnológica, Camino a la Presa San Jose# 2055, Col. Lomas 4a, CP. 78216 San Luis Potosí, Mexico*

ARTICLE INFO

Article history:
Received 23 September 2019
Accepted 27 March 2020
Available online 30 April 2020

Keywords:
Spark plasma sintering
Mechanical alloying
Titanium alloys
Phase transitions
Powder consolidation

ABSTRACT

A series of Ti–30Zr alloys have been synthesized by the spark plasma sintering (SPS) process using a mixture of elemental powders processed by mechanical alloying. A sintering temperature of 900 °C was used during SPS with heating rates of 140, 200 and 350 °C min^{-1} with a constant load of 50 MPa. The effect of the heating rate on the densification, microstructure, phase transformation and microhardness is discussed. The sintering kinetics and the in situ densification were performed by the analysis of the punch displacement during SPS processing. Structural details of consolidated materials were evaluated by the combination of X-ray diffraction, field emission scanning electron microscopy and differential scanning calorimetry tests. Vickers microhardness of samples was also evaluated. The results show that samples reached high densification values up to 99.7% of the relative density by using lower sintering temperatures in comparison to conventional sintering techniques. Phase transformation analysis demonstrates the formation of α″ and ω metastable phases without using any post-treatment. Microhardness values between 950 and 1040 HV were obtained as an effect of the SPS parameters and metastable phase precipitations.

1. Introduction

Commercially pure titanium (CP-Ti) and its alloys are one of the most used materials in engineering, petrochemical, automotive and aerospace applications due to combination of excellent mechanical properties and corrosion [1]. In addition, the excellent biocompatibility of these alloys make them ideal candidates in the biomedical field [2]. Besides these outstanding properties, Ti has been reinforced with additions of Ta, Nb and/or Zr, which present better biocompatibility and corrosion resistance in comparison to CP-Ti, and the highly used Ti6Al4V [3]. The addition of alloying elements into Ti allows to produce changes in the microstructure and mechanical response of the resultant alloys. Alloying zirconium to Ti has been

* *Corresponding author.*
E-mail: luisra24@gmail.com (L. Olmos).
https://doi.org/10.1016/j.jmrt.2020.03.110

continuously used in order to develop new biomedical and structural alloys with high mechanical strength, improved biocompatibility with small tendency to segregation during melting [4–6]. Also, it has been reported that Ti–Zr alloys improve the corrosion resistance by presenting a better oxide stability and passivation behavior than CP-Ti [7].

In terms of phase stabilization, the addition of alloying elements to CP-Ti and the processing parameters affect directly the microstructural characteristics and mechanical properties of the final alloy [8]. For example, the addition of carbon to a Ti matrix produce the stabilization of α-Ti phase and the increment of mechanical properties after a thermal processing [9], while the addition of β-stabilizers such as Ta or Nb decreases the strength and the elastic modulus of the matrix [10–13]. On the other hand, depending on the processing conditions, β-stabilized Ti alloys are susceptible to precipitate metastable phases such as the martensitic α′ and α″ with a deformed close-packed hexagonal (P63/mmc), and orthorhombic (*Cmcm*) lattices respectively, and also, ω-phase with hexagonal lattice (*P6/mmm*) [14]. The study of formation–decomposition mechanism, and the properties of the mentioned metastable phases helps the understanding of alloys behavior under conditions at which they would be submitted in different applications, improving the performance of materials in each device.

Martensitic α′/α″ phase formation in CP-Ti and Ti-based alloys occurs during the rapid cooling (quenching), from the high-temperature β-Ti phase taking place at the prior β-Ti grain boundaries by effect of a shearing process [15]. The start temperatures of the $\beta \rightarrow \alpha'/\alpha''$ transformation is lowered as an effect of the increment in the content of alloying elements, mainly those elements acting as β-stabilizers. For example, it has been reported that martensitic phases are obtained with up to 2 at.% of Mo content in the Ti–Mo binary alloy, while 9 at.% of Ta in Ti–Ta alloys, and 6 at.% of Nb in Ti–Nb system are needed [10]. This behavior can be considered in cases when the preservation of the properties of these phases is desirable [10,16,17]. Also, the decrease in microhardness and elastic modulus of alloys presenting an α″ microstructure have been reported [18,19]. In fact, it is mentioned that the α″ martensite has similar or lower modulus than β-Ti phase in some Ti alloys such as Ti–29Nb–13Ta–4.6Zr [20]. In addition, the mechanical properties of similar materials presenting martensitic microstructures can be influenced by the fabrication process, as it was reported for a selective laser melted (SLM) Ti6Al4V alloy which had a higher yield strength and less ductility than the same material fabricated by the wrought process [21].

The $\beta \rightarrow \omega$ transformation, which is not a martensitic type transformation, also deserves consideration in the phase analysis of Ti-based alloys. The precipitation of ω-phase in Ti alloys has been studied by Fontaine et al. [22] and Duerig et al. [23], they classified the ω-phase into two types, depending on their kinetics: first, the athermal phase (ω_{ath}), which is formed during cooling due to the instability of ⟨1 1 1⟩ planes of the β-phase, leads to a reordering of the planes resulting in a structural transformation into a hexagonal cell (*P6/mmm*). Then, a diffusional formation of the called isothermal phase (ω_{iso}) is carried out, which is formed during isothermal aging at low temperatures (<450 °C). Pearson [24] reported that the ω-phase lattice parameters are: $a = 4589$ Å and $c = 2.822$ Å. This was recently proved by Dubinskiy et al. [25] who concluded that both; ω_{ath} and ω_{iso} phases have similar $c/a = 0.613 \pm 0.003$. Additionally, it has also been reported that $\alpha \rightarrow \omega$ transformation through special mechanisms is also possible in pure Ti and Ti-based alloys, which is a product of the pressure application (in a range of 2–9 GPa, approximately) and is influenced by the temperature [26–30]. On the other hand, the reverse transformation $\omega \rightarrow \beta$ in CP-Ti can be attained by inducing stress of approximately 120 GPa [31]. In this regard, the decomposition of the ω-phase was investigated at temperatures above 375 °C [29]. Further, several characteristics of ω-phase were investigated, for example; it has been mentioned that this phase can strength the Ti alloys via the precipitation strengthening mechanism, as well as nucleation of the α-Ti phase [25,32]. Additionally, although both types of ω-phase (athermal or isothermal) are able to cause embrittlement of Ti alloys, this effect results negligible when the size of ω precipitates is fine (about 3 nm), which could even improve the shape memory and superelastic properties of the alloy [33].

Recently, the demand of Ti-based alloys has increased in spite of their high cost and different fabrication techniques, powder metallurgy (PM) is a technique that offers the best cost-effective processing due to minimum post-machining costs [34]. Among the conventional powder metallurgy techniques, spark plasma sintering (SPS) is a novel sintering technique which offers a rapid consolidation of fully dense materials [35,36]. SPS technique has been used to fabricate pure Ti [37] and Ti-based materials such as Ti–Ta–Ru alloys [38], Ti6Al4V–TiN composites [39], Ti–Nb alloys [40], among others. The high density attained is an effect of the continuous load assisted during sintering. These materials normally showed the effect of the high rate cooling on their microstructure, which is characterized by fine lamellae precipitated in the prior β grains and the increasing of phase stabilization according to the type of element added. As a comparison, Ti64/TiN composites fabricated using SPS [39] presented an apparent lower TiN diffusion than conventionally sintered Ti64/TiN materials [41] because of the difference in diffusion time and temperature. Moreover, to the best of the author knowledge, the information regarding Ti–Zr-based alloys fabricated through out SPS is limited to Ti alloys containing Zr and other elements [3,42,43]. Hence, the effects of SPS process on the microstructure and mechanical properties of binary Ti–Zr alloys must be clearly understood in order to elucidate the behavior of Ti–Zr-based alloys and their microstructural evolution. The aim of this study is to fabricate Ti–30Zr binary alloys by using SPS. In a first step, the preparation by mechanical alloying of raw material and analysis of the resulted mixture is performed. During SPS processing of mechanical alloyed powders, the effect of heating rate on the sintering kinetics and densification are studied. In addition, the effect of SPS parameters on the microstructure, phase decomposition and microhardness of the sintered alloy is also analyzed.

2. Materials and experimental procedure

In this investigation, Ti and Zr (>99.9% purity) powders were used as starting materials. Materials were mixed in an atomic percentage of 30 at.% Zr and 70 at.% Ti. The mixture was

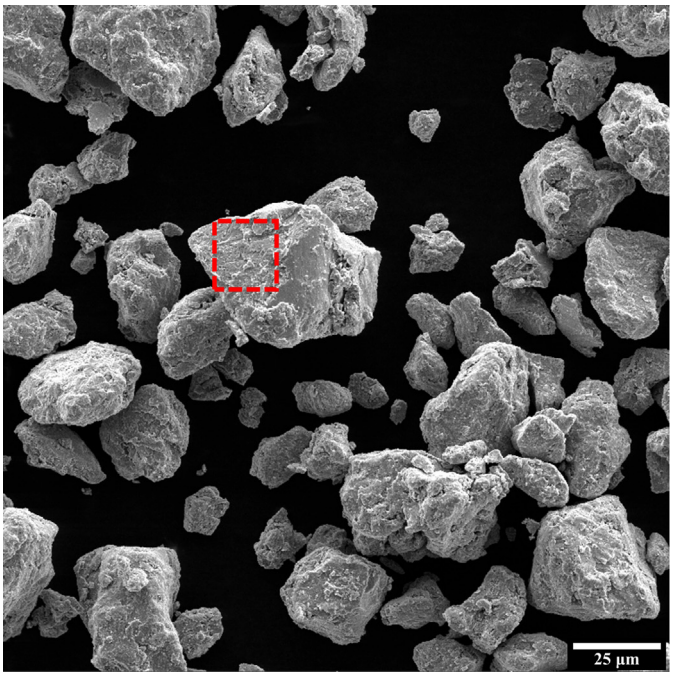

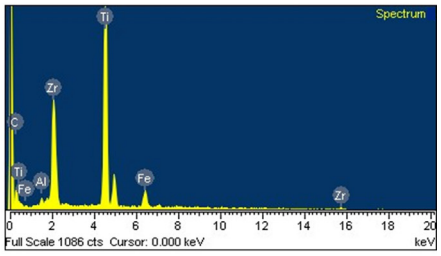

Element	Atomic %
Al K	1.86
Ti K	69.93
Fe K	8.14
Zr L	20.08
Total	100.00

Fig. 1 – SEM image and EDS analysis of mechanical alloyed Ti–30Zr powders.

mechanically milled in an O_1 steel vessel with stainless steel balls with a hardness of 61 HRC to give a ball to powder weight ratio of 10:1. The vial was sealed and evacuated at a vacuum pressure of 15 MPa. A planetary mill machine (RETSCH PM 400) was used for the milling at 200 rpm during 8 h. Mechanically alloyed (MA) powders were weighed to fabricate samples of ~5 mm height and subsequently poured into a 10 mm diameter graphite die. Sintering was performed by a SPS system (Land Labox-210 SPS) applying a constant load of 50 MPa and a sintering temperature of 900 °C, under vacuum. This sintering temperature was selected since the maximum densification of samples is reached below this temperature according to the dilatometric data obtained from exploratory tests. Three different heating rates of 140, 200 and 350 were used. Samples were then cooled with a cooling rate of 230 °C min^{-1} under vacuum in the SPS chamber after sintering. The sample temperature and displacement of punch were recorded during the sintering process.

For further characterization, SPS samples were cross-sectioned in order to ensure the analysis in the perpendicular direction of the load application. Cross-sectional surfaces were superficially prepared by conventional metallographic techniques and etched with a Kroll solution: (3 mL HF:6 mL HNO_3:100 mL H_2O) to analyze the microstructure. MA powders and SPS samples were analyzed in terms of structure by means of X-ray diffraction (XRD) at room temperature by using an Emperyan Panalytical diffractometer using K-alpha copper radiation with an energy of 30 kV and 30 mA, 0.2 step size, and a 1 s time step in a 2θ range of 30–90°. Microstructural and compositional analysis of both; MA powders and SPS samples were also carried out by using a Mira3 TESCAN field-emission scanning electron microscope (FE-SEM) and an XFlash® 6|30 Bruker energy dispersive spectroscopy detector (EDS), respectively. Phase evolution was analyzed by means of differential scanning calorimetry (DSC) with heating rates of 5, 15, 20 and 25 °C min^{-1} under Ar atmosphere by using a PerkinElmer Simultaneous Thermal Analyzer (STA) 6000, whereas Vickers microhardness values for SPS samples were obtained using a Future Tech FM-800 microhardness tester with a load of 300 g and 20 s of dwell time for each indentation.

3. Results and discussion

3.1. *Powders characterization*

Fig. 1 shows FE-SEM micrographs of the MA Ti–30Zr powders and their elemental composition analyzed by EDS of a selected particle. This result is representative of the analysis performed in 10 different particles. After mechanical alloying, the resulting particles presented angular shape with sizes below 30 µm, approximately. Composition analysis reveals the presence of Ti and Zr elements in similar atomic percentages of MA particles than in the initially designed mixtures. Fe amount increased from the released particles of the steel balls and the walls of the vessel during milling.

X-ray diffraction patterns of Ti and Zr raw materials and MA Ti–30Zr powders are shown in Fig. 2. The patterns are vertically shifted for better comparison. As shown in Fig. 2, raw materials (curves a and b) present diffraction peaks of hcp α-Ti and hcp α-Zr, respectively, both recognized as the low-temperature phases of each element [44,45]. On the other hand, the pattern of MA powders (curve c) is formed mainly by α-Ti and α-Zr peaks. α-Zr peaks shifts to higher diffraction angle indicating the deformation of the crystal cell due to relatively high-energy impacts during mechanical alloying. In addition, peaks of the cubic β-Ti phase (PDF 88-2321) resulted from the phase transformation during the heating caused

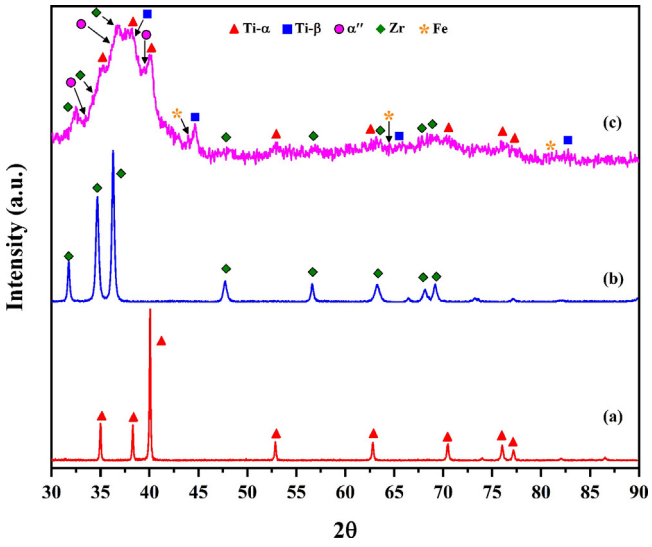

Fig. 2 – X-ray diffraction patterns at room temperature of (a) CP-Ti and (b) Zr initial materials and (c) MA Ti–30Zr powders.

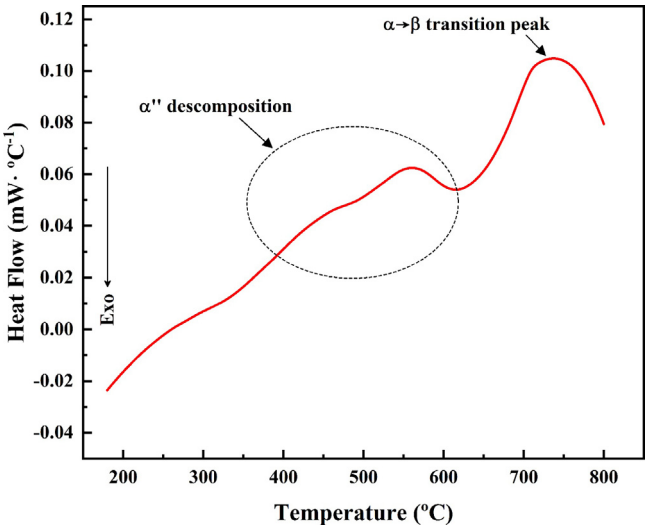

Fig. 3 – DSC curve of MA Ti–30Zr powders.

in the milling process. Some factors such as the operating frequency and ball/powders ratio influence the temperature reached inside the vessel during mechanical milling, which can reached up to 600 °C [46,47]. Thus, solid solution occurs at relatively low temperatures during mechanical alloying due to the generation of crystalline defects in powders caused by friction and high-energy impacts inside the vessel [48]. Broadening of diffraction peaks was seen after mechanical alloying as an effect of the crystallite size reduction and as a result of induced strain in the lattice [48,49]. Additionally to peak broadening, some reflections of the α-Ti martensitic phase (α″) were detected between the main α-Ti and α-Zr peaks, indicating that the energy generated during mechanical alloying was high enough to achieve the martensitic transformation of Ti [14,50]. Small reflections corresponding to the cubic Fe (PDF 85-1410) are also observed as a consequence of mechanical alloying.

In order to evaluate the phase transitions occurred during the heating in the sintering process, a DSC curve of MA Ti–30Zr powders for a heating rate of 10 °C min^{-1} is presented in Fig. 3. This figure shows two endothermic peaks between 400 and 650 °C and indicates that the reversible phase transformation of the α″ martensite obtained during the MA of powders into α + β metastable phase was achieved. Detected reaction peaks proved the existence of α″ after mechanical alloy of Ti–30Zr powders and the mentioned phase decomposition will be clarified later.

Further heating at 730 °C, resulted in an endothermic peak corresponding to the α/β transition. Detection of a lower transition temperature than the nominal for CP-Ti indicates the diffusivity between components in the alloy. According to the Ti–Zr equilibrium diagram [51], Zr is in constant solid solution with Ti in both; α and β phases, also, Zr is well known as a neutral element in terms of stabilizing Ti phases. However, it has been observed that a β-stabilizing effect of Zr directly depends on the content of the other β-stabilizing elements and impurities, since Zr increased the compositional ratio of β-stabilizing/Ti in the alloy [52]. EDS results of a conventional sintered Ti–13Nb–13Zr alloy revealed that the Zr content in the β phase is higher than in the α phase, suggesting its β-stabilizing effect [53].

3.2. *Sintering analysis*

In order to analyze the effect of the heating rate on the sintering kinetics of a Ti–30Zr alloy, some considerations must be taken. Assuming that the mass is constant during the whole sintering cycle, the in situ density of the samples can be obtained from:

$$\rho_i = \frac{m}{V_i} \quad (1)$$

where ρ_i is the instantaneous density, m is the mass of the sample and V_i is the instantaneous volume of the compact. The instantaneous volume depends on the densification during sintering and is estimated from the displacement of the graphite punch. As the sintering proceeds inside the graphite die, the radial displacement is null due to the rigidity of the die walls.

The relative density (D) is defined as the weight density of the compact divided by the theoretical density of the Ti–30Zr alloy at room temperature and can be estimated during the whole sintering cycle as follows:

$$D = \frac{\rho_i}{\rho_t} \quad (2)$$

where ρ_t is the theoretical density calculated by considering the rule of mixtures: $\rho_t = \rho_1 f_1 + \rho_2 f_2$, where ρ_1 and ρ_2 are theoretical densities and f_1 and f_2 are volume fraction of each component in the alloy.

Densification and densification rates curves as a function of the temperature for the different heating rates are shown in Fig. 4a and b, respectively. The onset of sintering is indicated by the change in the densification curves observed

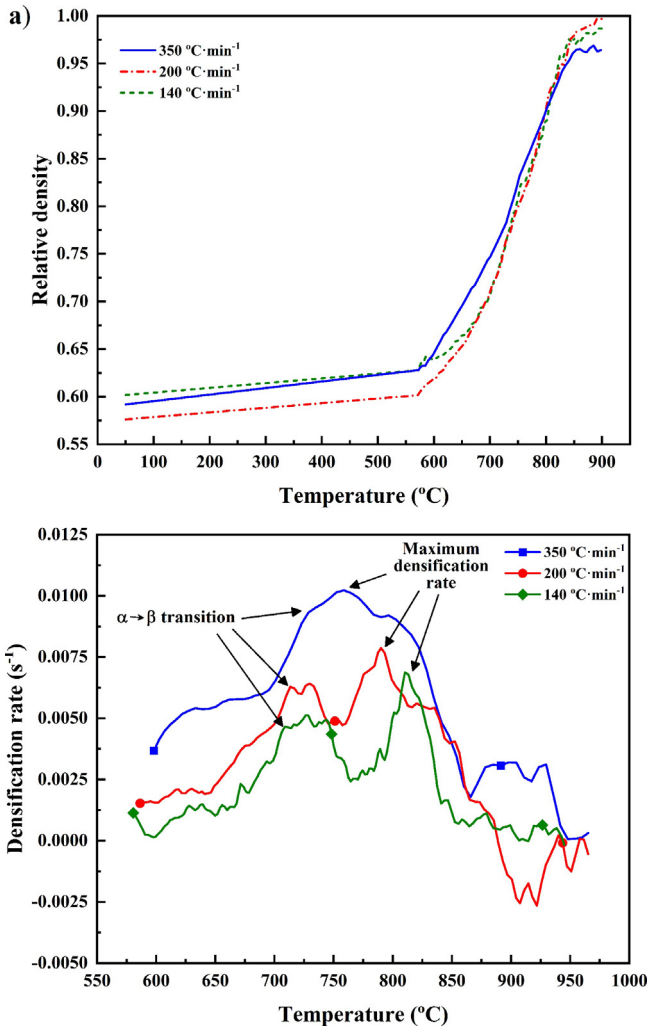

Fig. 4 – (a) Relative density and (b) densification rate as a function of the temperature during sintering of Ti–30Zr powders.

at 570 °C for the three heating rates used. The sintering of samples proceeds by increasing the relative density up to their maximum values of 98%, 99% and 96%, reached at 899, 893 and 884 °C for samples sintered with heating rates of 140, 200 and 350 °C min^{-1}, respectively. These results indicate that the increase in heating rate slightly decreased the temperature at which maximum densification was seen. In addition, the maximum densification values tend to decrease with the increment in heating rate. As the diffusion in a sintering process is time and temperature dependent, it is assumed that a faster sintering temperature decreases the diffusion time, which also reduces the densification level. Samples sintered at 140 and 200 °C min^{-1} showed a very similar densification behavior since there is not a considerable difference between their heating rates, hence, the small variation observed between their maximum densification values is attributed to the differences in number of contacts between particles. Relative density values obtained here are slightly higher than those observed for CP-Ti powders sintered with a heating rate of 100 °C min^{-1}, a pressure of 50 MPa and 900 °C [37].

The instantaneous densification rate $\dot{D}$ can be estimated as follows [54]:

$$\dot{D} = \frac{dD_i}{dt_i} = \frac{D_i - D_{i-1}}{t_i - t_{i-1}} \quad (3)$$

where D_i is the instantaneous relative density at the time t_i (s), for an interval of $t_i - t_{i-1}$ of 1 s. As it is observed in Fig. 4b, the densification rate values of the samples increases with the heating rate used for sintering, attaining the maximum value of 0.01 s^{-1}. These values resulted higher than those reported for the sintering of Ti and Ti6Al4V milled powders [55] and crystalline $Ti_{40.6}Zr_{9.4}Cu_{37.5}Ni_{9.4}Al_{3.1}$ powdered alloy [54]. Two peaks are detected in the curves of densification rates obtained at different heating rates. The first peak is attributed to the Ti phase transition, which is observed in a range of 700–750 °C for all samples. The width of the phase transition phase peaks decreases as an effect of the heating rate. In addition, variations due to the amplitude at the top of the transition peaks in samples sintered at 140 and 200 °C min^{-1} make difficult the determination of the precise phase transitions temperatures. Taking the first change in trend of densification rate as a reference, the phase transition temperatures are detected at 708, 713 and 728 °C for the samples sintered with 140, 200 and 350 °C min^{-1}, respectively. Hence, the effect of the heating rate can be estimated from the phase transition temperature. A similar effect has been found to determine the transition temperatures of low-carbon steel by means of dilatometric analysis [56]. The phase transition temperatures during sintering are very similar to those observed in DSC analysis of the Ti–30Zr powders (Fig. 3). Nevertheless, the thermal treatment is influenced by the pressure assistance in the SPS system, thus, tests using different loads during sintering are required in order to determine the load effect on the phase transition temperature of the alloy during SPS sintering.

The second peak represents the maximum of the densification rate reached for each sample. As it can be seen, this is affected by the heating rate during sintering, denoting that its increment reduces the temperature at which this maximum is attained. This effect is attributed to the fact that a higher heating rate gives the caloric energy to reach more quickly the maximum densification level of the samples, which is approximately 90% for sintered materials.

In order to estimate the activation energy during sintering, it should be taken into account that the spark plasma procedure induces the viscous flow to redistribute the matter inside the compact, where the viscosity is directly influenced by the sintering temperature. The first model to estimate the shrinkage under a viscous flow was proposed by Frenkel [57].

$$\frac{\Delta t}{l_0} = \frac{3\gamma}{4\emptyset\eta} t \quad (4)$$

where $\Delta l/l_0$ is the axial shrinkage of the compact, γ the surface energy, η the viscosity of material, Ø the particle diameter and

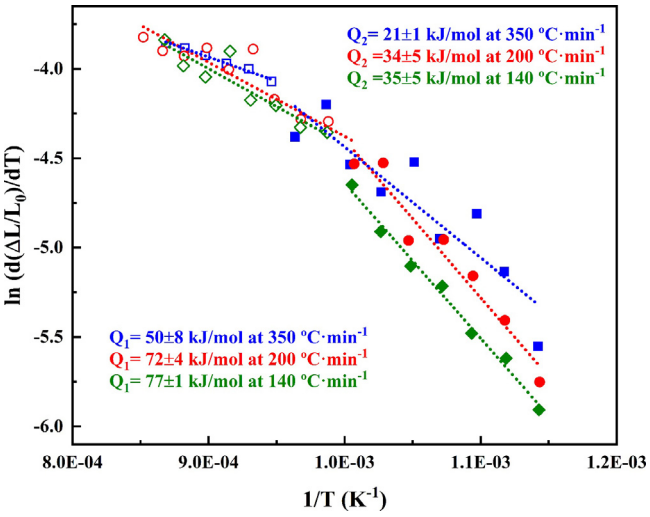

Fig. 5 – Arrhenius plot of $\ln(d(\Delta l/l_0)/dT)$ versus $1/T$ of Ti–30Zr powders sintered with different heating rates.

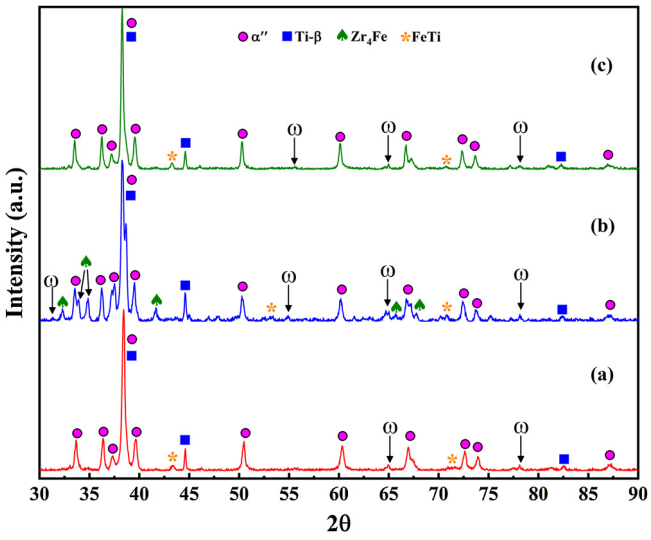

Fig. 6 – XRD patterns at room temperature of 350 °C Ti-30Zr SPS samples sintered with heating rates of (a) 140, (b) 200 and (c) 350 °C·min^{-1}.

t the time. Viscosity follows an Arrhenius relationship over a range of temperatures as follows:

$$\eta = \eta_0 \exp\left(\frac{Q}{RT}\right) \tag{5}$$

where η_0 (Pa s) is the viscosity coefficient, Q is the activation energy, R is the universal gas constant (8.314 J/mol) and T the temperature (K). Eq. (5) is possible to be written as [54,55]:

$$\ln\left(\frac{d(\Delta l/l_0)}{dT}\right) = \ln\left(\frac{3\gamma}{4\emptyset\eta_0}\right) - \frac{Q}{RT} \tag{6}$$

The Arrhenius plot of $\ln(d(\Delta l/l_0)/dT)$ vs $1/T$ for the sintered samples with different heating rates can be plotted as shown in Fig. 5. To calculate the value of Q, a linear regression is performed, and the value of the slope of the points corresponds to Q/R, meanwhile, the frequency factor can be obtained from the intercept. In Fig. 5, a break point of the straight line between 740 and 780 °C is clearly observed depending on the heating rate, indicating two different slopes which represent the activation energy in both α-Ti (Q_1) and β-Ti (Q_2) temperature ranges. It was found that the values of Q for β-Ti is approximately the half of the values of Q for α-Ti regardless of the heating rate. A similar trend of Q for α and β phases of Ti was reported before for micrometric Ti powders been analyzed by dilatometry at a heating rate of 10 °C min^{-1} [58]. In Fig. 5, the activation energy decreases with the heating rate increment for both; α-Ti or β-Ti phases, which is in agreement with the energy activation behavior reported elsewhere for Ti and Ti alloys sintered by SPS [54]. According to the viscosity equation proposed by Olevsky et al. [59], in which the viscosity coefficient (η_0) of 0.49 is used for Ti (Eq. (5)), a reduction in the activation energy represents a decrease in the viscosity during sintering.

3.3. *Characterization of samples*

X-ray diffraction patterns of the Ti–30Zr samples sintered with heating rates of 140, 200 and 350 °C min^{-1} are shown in Fig. 6. Unlike the MA powders, the crystallinity of phases in SPS samples increases as an effect of the heat treatment during sintering, allowing the definition of the diffraction peaks. As it can be observed, patterns are mainly constituted by α″ and some stabilized β-Ti. It has been mentioned that the martensitic transformations (α′ and α″) do not occur in the Ti–Zr system when the Zr amount is relatively low (8.4 and 14.6 at.% Zr). However, it alluded that the β stabilized systems such as Ti–Ta, Ti–V are able to transform to a martensitic phase during cooling [51,60]. For example, the formation of metastable martensitic α″ phase has been obtained in the arc-melted Ti–20Zr–10Nb [33] and Ti–30Zr–xNb (x = 5–13 at.%) [61] alloys, both alloys were annealed similarly in a range of 600–800 °C and then water quenched. Similar martensitic β → α″ has resulted from the quenching of a high Zr-containing Ti-based alloy (50 wt.% Zr), been emphasized by the induction of mechanical stresses attained from cold rolling of the alloy [62]. On this context, it has been reported that additions of only 2 wt.% of β-stabilizer Mo into a Ti–50Zr alloy is insufficient to obtain metastable α″ phase but, higher amounts as 2.5 wt.% increased the stability of the mentioned phase [63]. On this investigation, the slight addition of Fe during the mechanical alloying process increases the β-stabilizing effect of Zr allowing the presence of some reflections of retained β-Ti after SPS process of the Ti–30Zr alloy, see Fig. 6.

On the SPS process, the pressure assisting the sintering process has a strong influence on the structure of the final materials. Motsi et al. [37] showed the effect of pressure and temperature on the structure of CP-Ti during SPS process. They observed that by using temperatures below the phase transition temperature, the pressure had a negligible effect on the structure, but using higher temperatures than the β-transus,

the pressure has an effect on the structure decreasing the cell parameters of α-Ti.

Reflections corresponding to the ω-phase were recognized in XRD patterns of Fig. 6 indicating the presence of a small quantity of such phase in the Ti–30Zr alloy after sintering. Murray [51] referred to the ω-phase as a transition structure between the high-temperature β phase and the low-temperature α-phase in both; titanium and zirconium. The collapse of any pair of the (1 1 1) planes along the $[1\,1\,1]_{\beta}$ direction into a common plane to form a hexagonal structure of symmetry *P6/mmm*, which could even present an incomplete transformation into a trigonal rather than hexagonal. Moreover, it has been suggested that ω precipitates due to the relaxation of the strain caused by the volume expansion of crystalline lattice during quenching [64]. Additionally, the formation of ω-phase is often related to the metastable β titanium alloys, and is referred to one of the main causes of hardening of alloys [61]. ω-Phase was observed in a Ti–Nb alloy quenched from aging between 150 and 300 °C. The precipitation of the ω phase was proved by both; the appearance of its characteristic diffraction reflections, and hardening of alloys [65]. Similar results were found for the Ti–22Nb–6Zr system [25].

As it can be seen in the pattern b of Fig. 6, in SPS Ti–30Zr materials sintered at 200 °C min^{-1}, ω-phase diffraction peaks are more intense and easily detected. The increase in the intensity of peaks can be related to an increase in the amount of ω-phase in the sample regarding the samples sintered at 140 and 350 °C min^{-1}, which resulted from the higher β-Ti stabilization. Additionally, diffraction peaks of Zr_4Fe (PDF 18-0667) and FeTi (PDF 83-1635) intermetallics are detected on the patterns of Fig. 6 (curve b), while those peaks are hardly discernible in the other samples. The formation of intermetallic compounds between Zr and Fe [66–69], as well as between Fe and Ti [70,71] from different processes has been studied before.

In the analysis performed by Li et al. [60], the formation of the ω-phase was not detected in diffraction patterns of cold-rolled Ti–Zr alloy (30 and 50 at.% Zr) after annealing at 700 °C and water quenched. That alloy was prepared from pure materials by means of the arc-melting process, without prealloying or milling step. On the other hand, the ω-phase was detected by Qu et al. [61] in a Ti–30Zr alloy with different additions of Nb, fabricated by arc-melting and with a similar processing technique (with an annealing temperature of 600 °C). Likewise, Cui et al. [33] observed the formation of ω-phase from the annealing at temperatures between 600 and 800 °C of cold-rolled Ti–20Zr–10Nb alloy. Based on this evidence, the formation of the ω-phase appears to be enhanced by the addition of both; β-stabilizers and/or impurities to the Ti–Zr alloys.

Fig. 7 shows the FE-SEM images of the SPS Ti–30Zr samples sintered with different heating rates. The high densification level attained by samples can be appreciated from the reduced amount of porosity presented in the samples. On the other hand, the differentiation from the BSE images can be made since Zr acts as β-Ti stabilizer and increases the atomic number of that phase. α″ and β-Ti can be differentiated as the dark and bright phases, respectively. The effect of the heating rate is negligible on the microstructures of the samples sintered with 140 and 350 °C min^{-1} while a slight increase in the grain size of the sample sintered at 200 °C min^{-1} is observed. It has been demonstrated for arc-melted Ti–Zr alloys that the main microstructure obtained is a deformed α-Ti microstructure (α′/α″), which is a result of the difference in atomic radius between Ti and Zr, showing an acicular type microstructure which refines with the Zr content [60,72]. This type of microstructure is also presented in Ti–Zr based alloys with additions of β-stabilizers fabricated via melting since they promote the distortion of the crystal lattice [4,33,61,63]. The mentioned microstructure was also observed in a sintered Ti–13Nb–13Zr alloy which contains a balanced amount between Zr and Nb as β-stabilizer, even with a relatively slow cooling (furnace cooling) [53,73].

The microstructural features of the SPS Ti–30Zr alloy obtained in this research differ from those of the Ti–Zr based alloys fabricated by others techniques such as arc melting and conventional sintering, which showed acicular or fine plate-like α + β microstructures. The microstructures in our SPS Ti–30Zr materials is featured by equiaxed α-Ti grains precipitated in the β-Ti matrix. It is complicated to compare the microstructure of a Ti–Zr alloy resulted from melting and that obtained from an SPS process due to the marked differences in the processing. The conventional sintering process differs from SPS mainly in the pressure-assistance, and the high heating and cooling rates. On the other hand, the SPS Ti–13Nb–13Zr alloy investigated by He et al. [2] presented an equiaxed microstructure which is completely different to that showed by the same alloy fabricated by conventional powder metallurgy [53,73] and/or selective laser melting [74] which tend to be lamellar or acicular type. Additionally, the lack of previous reports regarding Ti–Zr alloys fabricated by the SPS technique becomes a challenging task to elucidate the obtained microstructure of a SPS Ti–Zr alloy. The α equiaxed microstructure obtained here is attributed to a recrystallization phenomenon promoted by both; the β-Ti phase stabilization effect of the Zr and the sintering conditions as the heating and cooling rates as well as the pressure assisting the sintering process.

3.4. *Phase transitions analysis*

The study of the decomposition of phases during heat treatments is really important not only to analyze the phase stability during thermal influence, but also to prove the presence of certain phases obtained during a prior process. Both objectives allow improving the further processes of materials, increasing their maneuverability for certain applications of these alloys. In order to analyze the reversible phase transformations of the SPS Ti–30Zr materials, DSC curves of tests with different heating rates of a sample sintered at 200 °C min^{-1} which are representative of the other samples are shown in Fig. 8. The corresponding phase transformation temperatures are listed in Table 1. A first endothermic peak is detected at 246 °C in the curve (a), corresponding to the transformation of the ω-phase (T_{ω}) into metastable α-Ti. Therefore, the analysis of the transition temperature of the ω-phase found here will be performed by comparison with the literature information as follows. The decomposition temperature of the ω-phase in SPS Ti–30Zr materials (T_{ω} = 246 °C) resulted higher than that reported for CP-Ti (107 °C) [27]. Other evidence for a Ti–30Zr with additions of Nb as β-stabilizer, the T_{ω} of the alloy increases from 309 to 334 °C with the addition of 7 and

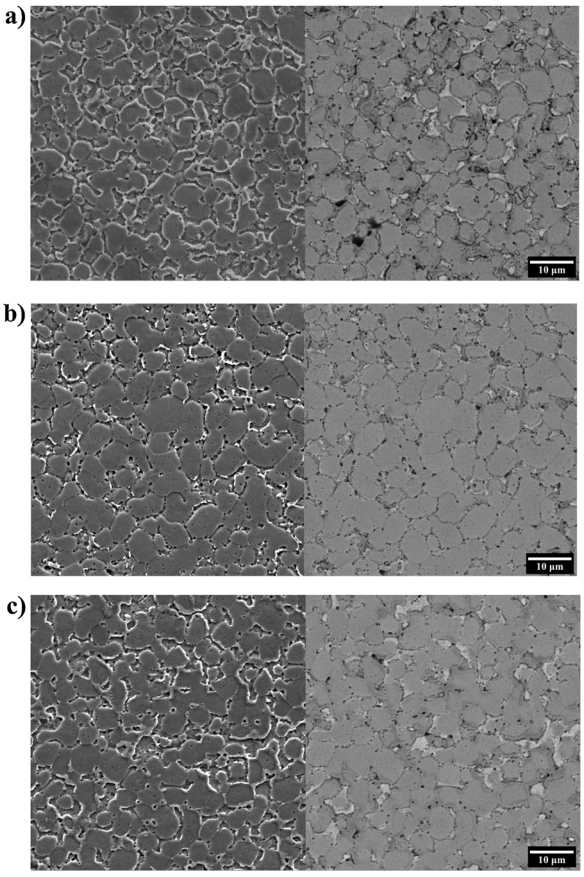

Fig. 7 – FE-SEM images of the SPS Ti-30Zr samples sintered with heating rates of (a) 140, (b) 200 and (c) 350 °C·min^{-1}. The figure on the left-hand side shows the secondary electron (SE) image while the figure on the right-hand shows side the back-scattered electron (BSE) image.

9 at.% of Nb, respectively [61]. Additionally, for a Ti–20Zr–10Nb alloy, the mentioned T_ω was 300 °C [33]. The comparison of the above-mentioned results with the T_ω for SPS Ti–30Zr materials obtained here, allow inferring that the T_ω depends on the β-stabilization degree in a Ti–Zr alloy.

Two peaks are observed in the curve (a) of Fig. 8 corresponding to the austenitic transformation of the martensitic α″ into metastable β-Ti with the start of transition temperature (A_s) of 346 °C and the final transition temperature (A_f) of 717 °C. The peaks identified as P1 an P2 represent the decomposition process as studied by Motyka et al. [15]. This process follows the scheme:

$$\alpha'' \rightarrow \alpha''_{en} + \alpha_M \rightarrow \alpha + \beta_M \rightarrow \alpha + \beta \quad (7)$$

where the martensitic α″ transform into a mixture of α″ enriched of the alloying elements which established the β-Ti and metastable α-Ti, as the transformation starts, P1. The maximum of the transformation is reached at A_{P1} and at the end of P1, a combination of α-Ti and metastable β-Ti is obtained. Subsequently, in P2, the metastable β-Ti transform into stable β-Ti at the maximum A_{P2} to form a mixture α + β, which further transformation expected is the transition to the high-temperature β-Ti phase.

Similarly to the ω-phase transformation, an effect of the heating rate used during the DSC tests on the austenitic transformation temperatures is observed. The increase in the heating rate in the tests produced the shift of the peak P1 to higher temperatures, while the peak P2 slightly shift to lower temperatures with the increasing heating rates. It seems that with the usage of higher heating rates both peaks will be unified, to show only one peak for the phase transition as most of the investigations reported. This phenomenon can be explained by the combination of both transitions when the first is not completed and the second transition stars due to the high heating rate. This behavior of onset temperature shift with the heating rate has been extensively studied by Saeed et al. [75]. In their work, the shift in transition temperatures is attributed to the rate of enthalpy change with the different heating rates, additionally, they suggested that the exploration of both; the optimal heating rate and sample mass would be performed in order to ensure the higher sensitivity for testing each material.

In this work, DSC tests at different heating rates were performed in order to investigate more accurately the transition temperature of the present phases in the SPS Ti–30Zr alloy. From the tests, it is possible to identify a decomposition temperature of the α″ in the range of 346 °C as the start

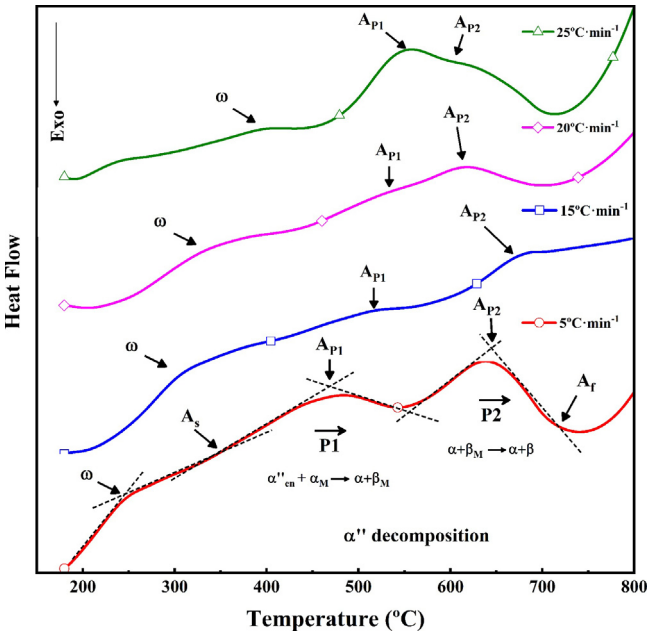

Fig. 8 – DSC curves of scans performed with heating rates of (a) 5, (b) 15, (c) 20 and (d) 25 °C min^{-1} of Ti–30Zr sintered with 200 °C min^{-1}.

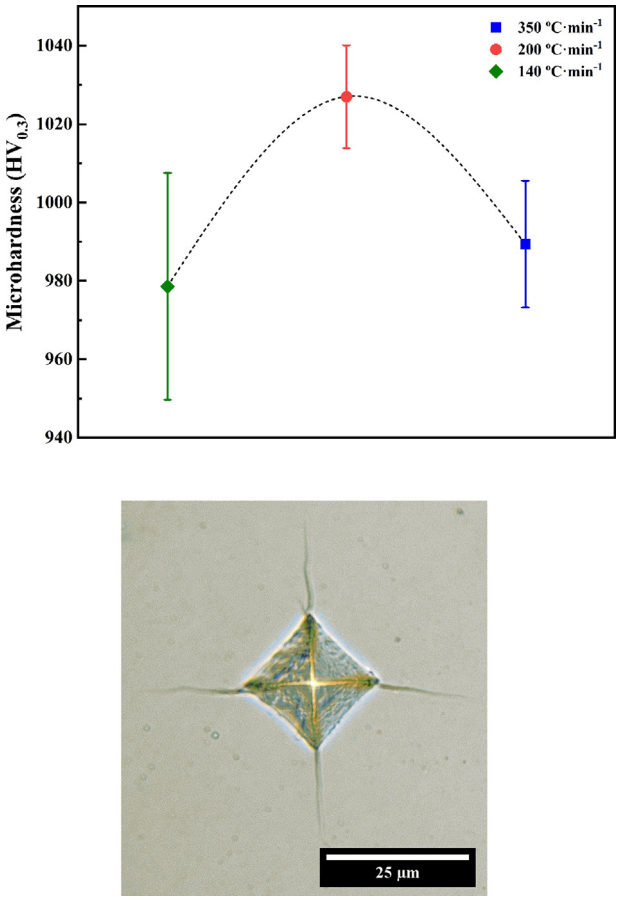

Fig. 9 – (a) Microhardness values of Ti–30Zr samples sintered by using different heating rates and (b) optical micrograph of a Vickers indentation on a Ti–30Zr sample sintered with a 140 °C min^{-1}.

of transformation to 717 °C as the end of the transformation, which narrows as the heating rate increase. In addition, it can be determined a maximum of the transformation temperature of 583 °C for the complete decomposition of α″ into stable α and β phases. It has been reported that the α″ martensite to β phase transition temperatures decreases with the addition of β-stabilizers to the Ti–Zr alloy, as seen in [29,41]. These results suggest that the increase in Zr content is rising the transition temperature, and on the other hand, the Nb amount is able to decrease the transition temperature. The increasing in transition temperature with the increment of Zr content was also proved for a melted Ti–Zr alloy [60].

3.5. *Microhardness analysis*

Fig. 9 shows the effect of the heating rate used during the SPS process on the microhardness of the Ti–30Zr alloy. As can be observed, the microhardness values of the three samples resulted in the range of 950 and 1040 HV. Samples sintered at 140 and 350 °C min^{-1} showed very similar values while the microhardness value of the sample sintered at 200 °C min^{-1} results slightly higher. The microhardness values obtained in this investigation resulted higher than the usual values for Ti–Zr alloys fabricated by means of melting, which ranks between 150 and 300 HV [72,76] and between 482 and 526 HV by the conventional powder metallurgy technique [77], depending on the Zr content. The differences between the microhardness values reached by means of both techniques can be explained by the efficiency in the diffusion between Ti and Zr during the process. It is believed that segregation occurs during melting of materials with different melting points, although remelting is performed to avoid that [78]. In the conventional powder metallurgy process, the high temperatures attained during the mechanical alloying and the sintering steps, enhance the diffusion of elements contributing to a better homogeneity of the alloy [49,77].

On the other hand, it is well known that the β-Ti has the lowest mechanical properties such as hardness and elas-

Table 1 – Phase transformation temperatures acquired at different heating rates for Ti–30Zr sample sintered with 200 °C min^{-1}.

Heating rate (°C min^{-1})	T_ω (°C)	A_s (°C)	A_{P1} (°C)	A_{P2} (°C)	A_f (°C)
5	246	346	468	645	717
15	323	416	513	676	717
20	343	451	521	616	685
25	397	471	546	593	695

tic modulus [79]. Nevertheless, in Ti–Mo system, the higher volume fraction of α″ phase in a Ti–7.5Mo alloy presented a microhardness almost 15% lower than the Ti–15Mo alloy, which showed a complete β-Ti microstructure [18]. Similar results were observed in Ti–Nb system in which the samples with α″ martensitic phase showed lower hardness than the materials with α′ and β-Ti microstructures, respectively [80]. However, this behavior is not presented by the SPS Ti–30Zr alloy studied here. The increase in grain size in the sample sintered at 200 °C min^{-1} suggests that the increment in the volume fraction of α″ is increasing the microhardness of the sample. The increment in microhardness of the α″ martensite can be due to the solid strengthening caused by the alloying of Zr to Ti, as previously seen for the Ti–50Zr–5Al–4V alloy [62]. Additionally, it is reported that the formation of ω-phase [33,65] and metastable phases can harden the Ti alloys [15,81]. The increment in the microhardness value of the SPS Ti–30Zr sample sintered at 200 °C min^{-1} in regard to the other samples can be attributed to the slight increase in the amount present of ω-phase and metastable Zr_4Fe and FeTi, as it was discussed above in Fig. 7.

An important factor to take into account for the explanation of the high microhardness obtained by the Ti–30Zr materials investigated in this work is the high densification level attained, which resulted as an effect of the high temperature, high heating and cooling rates, and the pressure assisting the sintering during the SPS process [37]. The Ti–20Nb–13Zr fabricated by Husseinn et al. [43] using SPS resulted almost near full dense with also high Vickers hardness (670 HV using 900 °C) denoting the effect of the SPS process in obtaining high hardness values. Those authors made a useful comparison of HV values of different types of Ti alloys fabricated by means of different sintering techniques. In their comparison, the alloys fabricated by using SPS attained higher hardness among similar alloys fabricated by means of conventional sintering techniques. Thus, composition can be the cause of the lower hardness values obtained by Hussein, as compared with the achieved hardness values for the SPS Ti–30Zr materials studied on this investigation.

In addition, it is well known that the properties of bulk materials can be influenced by the mechanical milling [82]. The possible effects of mechanical alloying process such as disorder of lattice and increase in dislocation density can effectively stress the lattice generating residual stresses and harden the particles [83]. It has been mentioned that materials fabricated by using ball milled powders showed hardness values considerably higher than alloys produced with pre-alloyed powders [84]. Since SPS is usually carried out under non-equilibrium conditions such as higher heating and cooling rates, the reordering of crystal lattice and residual stresses relaxation is not completely achieved during the sintering process leading to hardened materials. Cracks observed around indentations in Fig. 9b are often associated to brittle materials, which have higher hardness values [85]. Additionally, it has been reported that the increasing in cooling rate from the sintering temperature can improve the mechanical properties of a Ti alloy as an effect of a hardening process called “sinter hardening”, which occurs when sintered materials are quenched directly after the sintering step [86,87].

4. Conclusions

On this investigation, the effect of the heating rate on the sintering behavior of the Ti–30Zr alloy fabricated by means of the SPS process was studied. A microstructural characterization and the analysis of phase decomposition and microhardness of materials were performed in order to investigate the main features of the Ti–30Zr alloy synthesized by the SPS process. The main conclusions drawn from the results obtained are as follows:

High values of relative density up to 99.7% of the samples were attained by using the SPS processing. It was assessed that the activation energy for sintering and the phase transition temperatures increased with the heating rate while the maximum densification rate slightly decreased with the increment in the heating rate.

SPS Ti–30Zr alloys are mainly composed of equiaxed grains of α″ martensite precipitated into a β-Ti retained matrix. The SPS parameters also contributed to the precipitation of ω phase. A slight increase in α″ grain size was observed by using a heating rate of 200 °C·min^{-1}.

α″ and ω-phase decomposition temperatures obtained by DSC analysis were in agreement with the phase transition temperatures measured by displacement of the sample during SPS processing. The phase decomposition temperatures increased as an effect of the heating rate. This observation allowed to establish the optimum heating rate for this kind of tests (5 °C min^{-1}).

Microhardness values of the SPS Ti–30Zr materials resulted about 3 times higher than those obtained for the same alloy fabricated by other techniques as a result of the solid strengthening effect and the formation of both; metastable phases and intermetallic precipitations.

Conflicts of interest

The authors declare no conflicts of interest.

REFERENCES

[1] Chaudhari R, Bauri R. Microstructure and mechanical properties of titanium processed by spark plasma sintering (SPS). Metallogra Microstruct Anal 2014;3(1):30–5.
[2] He YH, Zhang YQ, Jiang YH, Zhou R. Microstructure evolution and enhanced bioactivity of Ti–Nb–Zr alloy by bioactive hydroxyapatite fabricated via spark plasma sintering. RSC Adv 2016;6(103):100939–53.
[3] Bertoli IR, Filgueira M, Ferreira LM, de Sousa LL, Mariano NA, Ramos AS, et al. Microstructure and corrosion behavior in SBF medium of spark plasma sintered Ti–xZr–20Si–10B (x = 5, 7, 10, 15, 20 at.%) alloys. J Alloys Compd 2019.
[4] Wang P, Feng Y, Liu F, Wu L, Guan S. Microstructure and mechanical properties of Ti–Zr–Cr biomedical alloys. Mater Sci Eng: C 2015;51:148–52.
[5] Cordeiro JM, Faverani LP, Grandini CR, Rangel EC, da Cruz NC, Nociti Junior FH, et al. Characterization of chemically treated Ti–Zr system alloys for dental implant application. Mater Sci Eng: C 2018;92:849–61.

[6] Perks C, Mudd G. Titanium, zirconium resources and production: A state of the art literature review. Ore Geol Rev 2019;107:629–46.
[7] Zhang Y, Davenport AJ, Burke B, Vyas N, Addison O. Effect of Zr addition on the corrosion of Ti in acidic and reactive oxygen species (ROS)-containing environments. ACS Biomater Sci Eng 2018;4(3):1103–11.
[8] Sinha A, Sanyal S, Bandyopadhyay NR. 2.11 thermal treatment for strengthening titanium alloys. In: Hashmi MSJ, editor. Comprehensive materials finishing. Oxford: Elsevier; 2017. p. 288–336.
[9] Adegbenjo AO, Olubambi PA, Westraadt JE, Lesufi M, Mphahlele MR. Interface analysis of spark plasma sintered carbon nanotube reinforced Ti6Al4V. JOM 2019, http://dx.doi.org/10.1007/s11837-019-03476-x.
[10] Kim HY, Miyazaki S. Martensitic transformation and superelastic properties of Ti–Nb base alloys. Mater Trans 2015;56(5):625–34.
[11] Dercz G. Structure and nanoindentation mechanical properties of novel porous Ti–Ta material with a core–shell structure using the powder metallurgy method. Adv Powder Technol 2019;30(5):1006–17.
[12] Xu S, Liu Y, Yang C, Zhao H, Liu B, Li J, et al. Compositionally gradient Ti–Ta metal–metal composite with ultra-high strength. Mater Sci Eng: A 2018;712:386–93.
[13] Chávez J, Jiménez Alemán O, Flores Martínez M, Vergara-Hernández HJ, Olmos L, Garnica-González P, et al. Characterization of Ti6Al4V–Ti6Al4V/30Ta bilayer components processed by powder metallurgy for biomedical applications. Metals Mater Int 2019.
[14] Barriobero-Vila P, Biancardi Oliveira V, Schwarz S, Buslaps T, Requena G. Tracking the α″ martensite decomposition during continuous heating of a Ti–6Al–6V–2Sn alloy. Acta Mater 2017;135:132–43.
[15] Motyka M, Baran-Sadleja A, Sieniawski J, Wierzbinska M, Gancarczyk K. Decomposition of deformed α′(α″) martensitic phase in Ti–6Al–4V alloy. Mater Sci Technol 2019;35(3):260–72.
[16] Konopatsky A, Brailovski V, Filonov M, Dubinskiy S, Zhukova Y, Korotitskiy A, et al. Manufacturing and characterization of novel Ti–Zr-based shape memory alloys. Mater Today: Proc 2017;4(3 Part B):4856–60.
[17] Kim HY, Fukushima T, Buenconsejo PJS, Nam T-h, Miyazaki S. Martensitic transformation and shape memory properties of Ti–Ta–Sn high temperature shape memory alloys. Mater Sci Eng: A 2011;528(24):7238–46.
[18] Ho WF, Ju CP, Chern Lin JH. Structure and properties of cast binary Ti–Mo alloys. Biomaterials 1999;20(22):2115–22.
[19] Inaekyan K, Brailovski V, Prokoshkin S, Pushin V, Dubinskiy S, Sheremetyev V. Comparative study of structure formation and mechanical behavior of age-hardened Ti–Nb–Zr and Ti–Nb–Ta shape memory alloys. Mater Charact 2015;103:65–74.
[20] Hao YL, Yang R, Niinomi M, Kuroda D, Zhou YL, Fukunaga K, et al. Young's modulus and mechanical properties of Ti–29Nb–13Ta–4.6Zr in relation to α″ martensite. Metallur Mater Trans A 2002;33(10):3137–44.
[21] Agius D, Kourousis IK, Wallbrink C. A review of the as-built SLM Ti–6Al–4V mechanical properties towards achieving fatigue resistant designs. Metals 2018;8(1).
[22] De Fontaine D, Paton NE, Williams JC. The omega phase transformation in titanium alloys as an example of displacement controlled reactions. Acta Metall 1971;19(11):1153–62.
[23] Duerig TW, Terlinde GT, Williams JC. Phase transformations and tensile properties of Ti–10V–2Fe–3Al. Metall Trans A 1980;11(12):1987–98.
[24] Pearson WB. A handbook of lattice spacings and structures of metals and alloys: International series of monographs on metal physics and physical metallurgy. Elsevier; 2013.
[25] Dubinskiy S, Korotitskiy A, Prokoshkin S, Brailovski V. In situ X-ray diffraction study of athermal and isothermal omega-phase crystal lattice in Ti–Nb-based shape memory alloys. Mater Lett 2016;168:155–7.
[26] Hennig RG, Trinkle DR, Bouchet J, Srinivasan SG, Albers RC, Wilkins JW. Impurities block the alpha to omega martensitic transformation in titanium. Nat Mater 2005;4(2):129–33.
[27] Jafari M, Vaezzadeh M, Noroozizadeh S. Thermal stability of α phase of titanium by using X-ray diffraction. Metallur Mater Trans A 2010;41(13):3287–90.
[28] Devaraj A, Nag S, Srinivasan R, Williams REA, Banerjee S, Banerjee R, et al. Experimental evidence of concurrent compositional and structural instabilities leading to ω precipitation in titanium–molybdenum alloys. Acta Mater 2012;60(2):596–609.
[29] Xiao JF, Nie ZH, Tan CW, Zhou G, Chen R, Li MR, et al. Effect of reverse β-to-ω transformation on twinning and martensitic transformation in a metastable β titanium alloy. Mater Sci Eng: A 2019;759:680–7.
[30] Dmitriev VP, Dubrovinsky L, Bihan TL, Kuznetsov A, Weber HP, Poniatovsky EG. Collapsed hexagonal ω-phase in a compressed TiZr alloy: Angle-dispersive synchrotron-radiation X-ray diffraction study. Phys Rev B 2006;73(9).
[31] Velisavljevic N, MacLeod S, Cynn H. Titanium alloys at extreme pressure conditions, titanium alloys-towards achieving enhanced properties for diversified applications. IntechOpen 2012.
[32] Zheng Y, Williams REA, Wang D, Shi R, Nag S, Kami P, et al. Role of ω phase in the formation of extremely refined intragranular α precipitates in metastable β-titanium alloys. Acta Mater 2016;103:850–8.
[33] Cui Y, Li Y, Luo K, Xu H. Microstructure and shape memory effect of Ti–20Zr–10Nb alloy. Mater Sci Eng: A 2010;527(3):652–6.
[34] Bolzoni L. Low-cost Fe-bearing powder metallurgy Ti alloys. Metal Powder Rep 2019.
[35] Liu S, Zhang G, Shi M, Yang X, Li A. Microstructure and properties of porous titanium prepared by spark plasma sintering. Metals 2019;9(1).
[36] Olevsky EA, Dudina DV. Field-assisted sintering: science and applications. Springer International Publishing; 2018.
[37] Motsi GT, Guillemet-Fritsch S, Chevallier G, Shongwe MB, Olubambi PA, Estournes C. Microstructural evolution and mechanical properties of pure titanium powders processed by spark plasma sintering. Powder Technol 2019;345:415–24.
[38] Obadele BA, Falodun OE, Oke SR, Olubambi PA. Spark plasma sintering behaviour of commercially pure titanium micro-alloyed with Ta–Ru. Part Sci Technol 2018:1–7.
[39] Falodun OE, Obadele BA, Oke SR, Maja ME, Olubambi PA. Effect of sintering parameters on densification and microstructural evolution of nano-sized titanium nitride reinforced titanium alloys. J Alloys Compd 2018;736:202–10.
[40] Karre R, Kodli BK, Rajendran A, Nivedhitha J, Pattanayak DK, Ameyama K, et al. Comparative study on Ti–Nb binary alloys fabricated through spark plasma sintering and conventional P/M routes for biomedical application. Mater Sci Eng: C 2019;94:619–27.
[41] Chávez J, Olmos L, Jiménez O, Bouvard D, Rodríguez E, Flores M. Sintering behaviour and mechanical characterisation of Ti64/xTiN composites and bilayer components. Powder Metall 2017;60(4):257–66.
[42] Rechtin J, Torresani E, Ivanov E, Olevsky E. Fabrication of titanium–niobium–zirconium–tantalium alloy (TNZT)

bioimplant components with controllable porosity by spark plasma sintering. Materials (Basel) 2018;11(2):181.
[43] Hussein MA, Suryanarayana C, Al-Aqeeli N. Fabrication of nano-grained Ti–Nb–Zr biomaterials using spark plasma sintering. Mater Des 2015;87:693–700.
[44] Kherrouba N, Bouabdallah M, Badji R, Carron D, Amir M. Beta to alpha transformation kinetics and microstructure of Ti–6Al–4V alloy during continuous cooling. Mater Chem Phys 2016;181:462–9.
[45] Cochrane C, Daymond MR. Effect of temperature and loading sense on deformation-induced phase transformation in a high Sn content zirconium alloy. Mater Sci Eng: A 2019;748:313–26.
[46] Schmidt R, Martin Scholze H, Stolle A. Temperature progression in a mixer ball mill. Int J Indus Chem 2016;7(2):181–6.
[47] Kwon Y-S, Gerasimov KB, Yoon S-K. Ball temperatures during mechanical alloying in planetary mills. J Alloys Compd 2002;346(1):276–81.
[48] Singh P, Abhash A, Yadav BN, Shafeeq M, Singh IB, Mondal DP. Effect of milling time on powder characteristics and mechanical performance of Ti4wt%Al alloy. Powder Technol 2019;342:275–87.
[49] Karouia A, Slama C, Jaafar H, Schoenstein F, Abdellaoui M, Jouini N. Microstructural and mechanical study of nanocrystalline (Ti0.8W0.2)C synthesized by high-energy ball milling. Int J Refract Met Hard Mater 2019; 83(1049):68.
[50] Flower HM, Davis R, West DRF. Martensite formation and decomposition in alloys of titanium containing β-stabilizing elements. In: Williams JC, Belov AF, editors. Titanium and titanium alloys: Scientific and technological aspects volume 3. Boston, MA: Springer US; 1982. p. 1703–15.
[51] Murray JL. The Ti–Zr (titanium-zirconium) system. Bull Alloy Phase Diagrams 1981;2(2):197–201.
[52] Abdel-Hady M, Fuwa H, Hinoshita K, Kimura H, Shinzato Y, Morinaga M. Phase stability change with Zr content in β-type Ti–Nb alloys. Scr Mater 2007;57(11):1000–3.
[53] Henriques VAR, Galvani ET, Petroni SLG, Paula MSM, Lemos TG. Production of Ti–13Nb–13Zr alloy for surgical implants by powder metallurgy. J Mater Sci 2010;45(21):5844–50.
[54] Liu LH, Yang C, Yao YG, Wang F, Zhang WW, Long Y, et al. Densification mechanism of Ti-based metallic glass powders during spark plasma sintering process. Intermetallics 2015;66:1–7.
[55] Yang C, Zhu MD, Luo X, Liu LH, Zhang WW, Long Y, et al. Influence of powder properties on densification mechanism during spark plasma sintering. Scr Mater 2017;139: 96–9.
[56] Vázquez-Gómez O, Gallegos-Pérez AI, López-Martínez E, Vergara-Hernández HJ, Barrera-Godínez JA. Criteria for the dilatometric analysis to determine the transformation kinetics during continuous heating. J Therm Anal Calorim 2018;135(6):2985–93.
[57] Frenkel J. Viscous flow of crystalline bodies under the action of surface tension. J Phys 1945;9:385.
[58] Dabhade VV, Mohan TRR, Ramakrishnan P. Viscous flow during sintering of attrition milled nanocrystalline titanium powders. Mater Res Bull 2007;42(7):1262–8.
[59] Olevsky E, Dudek HJ, Kaysser WA. Hiping conditions for processing of metal matrix composites using continuum theory for sintering–II. Application to fibre reinforced titanium alloys. Acta Mater 1996;44(2):715–24.
[60] Li Y, Cui Y, Zhang F, Xu H. Shape memory behavior in Ti–Zr alloys. Scr Mater 2011;64(6):584–7.
[61] Qu W, Sun X, Yuan B, Xiong C, Zhang F, Li Y, et al. Microstructures and phase transformations of Ti–30Zr–xNb (x = 5, 7, 9, 13 at.%) shape memory alloys. Mater Charact 2016;122:1–5.
[62] Shi YD, Wang LN, Liang SX, Zhou Q, Zheng B. A high Zr-containing Ti-based alloy with ultralow Young's modulus and ultrahigh strength and elastic admissible strain. Mater Sci Eng: A 2016;674:696–700.
[63] Zhang S, Liang SX, Yin YX, Zheng LY, Xie HL, Shen Y. Martensitic transition and shape memory effect of Ti–Zr–Mo series alloys. Intermetallics 2017;88:55–60.
[64] Barriobero-Vila P, Requena G, Warchomicka F, Stark A, Schell N, Buslaps T. Phase transformation kinetics during continuous heating of a β-quenched Ti–10V–2Fe–3Al alloy. J Mater Sci 2014;50(3):1412–26.
[65] Mantani Y, Tajima M. Phase transformation of quenched α″ martensite by aging in Ti–Nb alloys. Mater Sci Eng: A 2006;438–440:315–9.
[66] Burr PA, Murphy ST, Lumley SC, Wenman MR, Grimes RW. Hydrogen solubility in zirconium intermetallic second phase particles. J Nucl Mater 2013;443(1–3):502–6.
[67] Lumley SC, Murphy ST, Burr PA, Grimes RW, Chard-Tuckey PR, Wenman MR. The stability of alloying additions in zirconium. J Nucl Mater 2013;437(1–3):122–9.
[68] Yang WJS, Tucker RP, Cheng B, Adamson RB. Precipitates in zircaloy: Identification and the effects of irradiation and thermal treatment. J Nucl Mater 1986;138(2):185–95.
[69] Zavalii IY, Yurchyk M, Vovk OM, Saldan IV, Koval'chuk IV. Effect of high-energy milling on hydrogen desorption and the structure of mixtures of Zr-containing materials. Mater Sci 2005;41(6):772–6.
[70] Adelfar R, Mirzadeh H, Ataie A, Malekan M. Amorphization and mechano-crystallization of high-energy ball milled FeTi alloys. J Non-Cryst Solids 2019;520(1194):66.
[71] Zadorozhnyy VY, Klyamkin SN, Kaloshkin SD, Skakov YA. Production of intermetallic compound of FeTi by means of mechanical–chemical synthesis and its interaction with hydrogen. Inorg Mater: Appl Res 2010;1(1):41–5.
[72] Ho W-F, Chen W-K, Wu S-C, Hsu H-C. Structure, mechanical properties, and grindability of dental Ti–Zr alloys. J Mater Sci: Mater Med 2008;19(10):3179–86.
[73] Henriques VAR, d Campos PP, Cairo CAA, Bressiani JC. Production of titanium alloys for advanced aerospace systems by powder metallurgy. Mater Res 2005;8:443–6.
[74] Zhou L, Yuan T, Li R, Tang J, Wang G, Guo K, et al. Densification, microstructure evolution and fatigue behavior of Ti–13Nb–13Zr alloy processed by selective laser melting. Powder Technol 2019;342:11–23.
[75] Saeed RM, Schlegel J, Castano C, Sawafta R. Uncertainty of thermal characterization of phase change material by differential scanning calorimetry analysis. Int J Eng Res Technol 2016;5(1):405–12.
[76] Kobayashi E, Matsumoto S, Doi H, Yoneyama T, Hamanaka H. Mechanical properties of the binary titanium-zirconium alloys and their potential for biomedical materials. J Biomed Mater Res 1995;29(8):943–50.
[77] Slokar L, Štrkalj A, Glavaš Z. Synthesis of Ti–Zr alloy by powder metallurgy. Eng Rev 2019;39(1):115–23.
[78] Nguyen VT, Qian M, Shi Z, Song T, Huang L, Zou J. Compositional design of strong and ductile (tensile) Ti–Zr–Nb–Ta medium entropy alloys (MEAs) using the atomic mismatch approach. Mater Sci Eng: A 2019;742:762–72.
[79] Lütjering G, Williams JC. Titanium. Berlin Heidelberg: Springer; 2013.
[80] Lee CM, Ju CP, Chern Lin JH. Structure–property relationship of cast Ti–Nb alloys. J Oral Rehabil 2002;29(4):314–22.
[81] Zhu W-g, Li P, Sun X, Chen W, Zhang H-l, Sun Q-y, et al. Precipitation response and hardening behaviors of Fe-modified Ti5553 alloy. Trans Nonferrous Metals Soc China 2019;29(6):1242–51.

[82] Kozlík J, Stráský J, Harcuba P, Ibragimov I, Chráska T, Janeček M. Cryogenic milling of titanium powder. Metals 2018;8(1):31.
[83] Suryanarayana C. Mechanical alloying and milling. Prog Mater Sci 2001;46(1):1–184.
[84] Mavros N, Larimian T, Esqivel J, Gupta RK, Contieri R, Borkar T. Spark plasma sintering of low modulus titanium–niobium–tantalum–zirconium (TNTZ) alloy for biomedical applications. Mater Des 2019;183(1081):63.
[85] Keryvin V, Hoang VH, Shen J. Hardness, toughness, brittleness and cracking systems in an iron-based bulk metallic glass by indentation. Intermetallics 2009;17(4):211–7.
[86] Dlapka M, Danninger H, Gierl C, Lindqvist B. Sinter hardening – a special heat treatment for powder metallurgy precision parts. HTM J Heat Treat Mater 2012;67(3):223–31.
[87] Zhang F, Reich M, Kessler O, Burkel E. The potential of rapid cooling spark plasma sintering for metallic materials. Mater Today 2013;16(5):192–7.